Supplementary Information

Direct mapping of the solid-liquid adhesion energy with sub-nanometre resolution

Kislon Voïtchovsky, Jeffrey J. Kuna, Sonia Antoranz Contera, Erio Tosatti and Francesco Stellacci

Index of the Supplementary Information:

1. Supplementary experimental details

Samples preparation

a. Mica:

Mica substrates purchased from SPI (SPI supplies, West Chester, PA, USA) were glued to metallic discs (Ted Pella Inc, Redding, CA, USA) that can be magnetically attached to the scanner. The samples were cleaved immediately before being placed in the liquid cell for imaging. For mica imaging, lower quality mica (grade 3-4) was used in order to ensure the presence of surface defects to prove reliability of the high-resolution images.

b. Calcite

Several pieces of optical grade calcite (Iceland Spar) were cleaved with a razor blade according to the desired crystalline direction [10$\underline{1}$4] and incubated for several days in ultrapure water (18.2 MΩ, Millipore, Billerica, MA, USA) so as to allow the samples to equilibrate with the solution. The pH of the resulting solution was found to be 9.4±2, consistent with Liang et al.[1]. One of the samples was then glued to a metallic disc and imaged in the incubation solution.

c. Fluorite

Fluorite samples from the Yaogangxian mine (Hunan, China) were cleaved with a razor blade according to the desired crystalline direction [111] and incubated for several hours in ultrapure water. The samples was then glued to a metallic disc and imaged in the

incubation solution. The fluorite samples were not as optically clear as calcite samples, and generally presented more surface defects and/or impurities (Fig.2).

d. Other single crystals

All the other single crystals investigated were purchased from MTI (MTI corp., Richmond, CA, USA) and were EPI-polished according a predefined crystalline direction by the manufacturer. In order to ensure that no contamination affected the results, measurements on four crystals picked randomly were repeated (both with AFM and CA) after cleaning of the samples by successive sonication in DMSO, ethanol, acetone, ethanol and ultrapure water. No significant differences were observed in the imaging parameters and the W_{SL} obtained.

f. Lipid bilayers

All the lipids (1,2-dipalmitoyl-sn-glycero-3-phosphocholine (DPPC), 1,2-dihexadecanoyl-sn-glycero-3-phospho-L-serine (sodium salt) (DPPS) and 1,2-dihexadecanoyl-sn-glycero-3-phosphate (sodium salt) (DPPA)) were purchased from Avanti polar lipids (Avanti Polar Lipids, Inc., Alabaster, AL, USA) in a chloroform-based solution. We followed standard procedures for achieving supported bilayers on freshly cleaved mica[2]. In short, lipids were placed in a glass vial and dried under vacuum for ~8h. They were then dissolved in a 20mM NaCl solution (0.65 mM final lipid concentration) and sonicated above the transition temperature of the lipid. Subsequently 30 µl of the lipid solution was deposited onto freshly cleaved mica and incubated overnight at 4° C. The sample was then heated again for 45 min. above the transition

temperature of the lipids. Attention was paid to never allow the samples to dry. The samples were then allowed to cool and subsequently rinsed with 2ml of 20mM NaCl solution just before imaging in a same solution. Experiment carried out in standard PBS buffer solution also allowed molecular level resolution (see Fig. S3). Subsequent AFM imaging and nano-dissection of the bilayers (see Fig. S3) confirmed the presence of well formed bilayers over the mica substrate.

g. Mercaptohexanol self-assembled monolayer (MH SAM)

The MH SAM was prepared according to a procedure described elsewhere[3]. In brief, substrates of gold evaporated on mica (Agilent) were cleaned in piranha solution (3 parts sulfuric acid: 1 part hydrogen peroxide (30%)). The substrates were subsequently rinsed with water and ethanol, and dried under a nitrogen flow. The substrates were then placed in sealed vials containing 10 ml of ethanolic solution of 6-mercaptohexan-1-ol (mercaptohexanol, MH) (Sigma). The thiol concentration was 0.01 mM. The substrates were left in solution at room temperature for a period of 7 days, at which point they were cleaned with ethanol and dried under a gentle airflow. Contact angle measurements were taken on the substrates before they were mounted and used for AFM measurements. Previous unpublished studies indicate that SAMs prepared this way are mostly in the stand-up phase with few or no regions in the lie-down phase, as confirmed by the AFM images acquired.

2. Study of the role of the tip oscillation amplitude for high-resolution imaging of mica in water

Figure S1 presents complementary information to Fig. 1. Using the harmonic oscillator model[4-12] (see also[13-15] for new developments in liquid) the variation of energy dissipation E_{TS} and tip-sample interaction stiffness k_{TS} as a function of the average tip-sample distance can be calculated from the experimental parameters (namely phase and amplitude). Figure S1 (a) and (b) present respectively E_{TS} and k_{TS} for various free amplitudes (same amplitudes and nomenclature as in Fig. 1). Note the log scale in (a). The curves have been offset vertically in (b) to allow for better readability. In each case, as for the γ_{TS} curves in Fig. 1c, the tip to mica distance has been normalized by the tip free amplitude A_0 to allow better comparison between the curves, and the point corresponding to the best imaging parameters has been marked as "setpoint". This approach is motivated by the fact that γ_{TS}, k_{TS} and E_{TS} all depend on a ratio of A and A_0. For all the curves this ratio will converge from a same initial value (at large tip-sample distances when $A=A_0$) to a same final value (at very short distances when $A\rightarrow 0$) over a tip-sample distance typically proportional to A_0. This is because when approaching the sample, a tip oscillating with an amplitude A_0 will already "touch" the sample at an average tip-sample distance of $A_0/2$. Consequently, normalizing the tip-sample distance to A_0 yields a similar damping distance for all the curves, regardless of the initial oscillation amplitude. A given value of normalized height then corresponds to a similar A/A_0 for all the curves thus allowing direct comparison.

The two regimes discussed for the γ_{TS} vs distance curves are also apparent in the E_{TS} vs distance curves (Fig. S1 a). For amplitudes smaller than $A_{0,\,optimum}$, the E_{TS} curves present

a simple monotonic increase as the vibrating tip approaches the surface, interpreted as a full damping of the vibration into the interfacial liquid. As the amplitude increases, the E_{TS} curves become bi-modal with a new, larger, maximum appearing near 0.1 interpreted as due to dissipation into the mica substrate. The energy dissipation curve corresponding to $A_{0,\,optimum}$ is here again at the transition between the two regimes. We note that in each case, the energy dissipation was arbitrarily set to zero ($\varphi=\pi/2$) away from the interface (tip oscillating in the bulk liquid). This approach allows better comparison between the different sets of parameters studies by setting a reference point. Under such circumstance E_{TS} does not represent the absolute energy dissipation but rather the increase of energy dissipation as the tip approaches the interface. The interaction stiffness k_{TS} increases almost linearly in each case with larger amplitudes providing stiffer interactions (b). As the amplitude reaches $A_{0,\,optimum}$, k_{TS} exhibits similar behaviour in the region attributed to the interfacial liquid. The stiffness then tends to increase steeply close to the mica (e.g. close to zero for the green curve, A_0=1.25 nm or in Fig. S2) although this is not obvious for all curves in Fig. S1 due to some instability of the tip oscillation and a low signal/noise ratio at very short distances (<0.1). Figure S1c complements Fig. 1b with more images of mica captured at different amplitudes. When the amplitudes become close to $A_{0,\,optimum}$, the mica lattice[16,17] becomes visible. The raw data (amplitude and phase vs distance curves) is presented in (d) and (e) respectively. The curves are the average of capture series in each case. The scale in (d) is semi-logarithmic and the minimum of the curves has been set to zero. All the curves have been aligned based on the corresponding deflection vs distance curves (not shown) and the zero set arbitrarily.

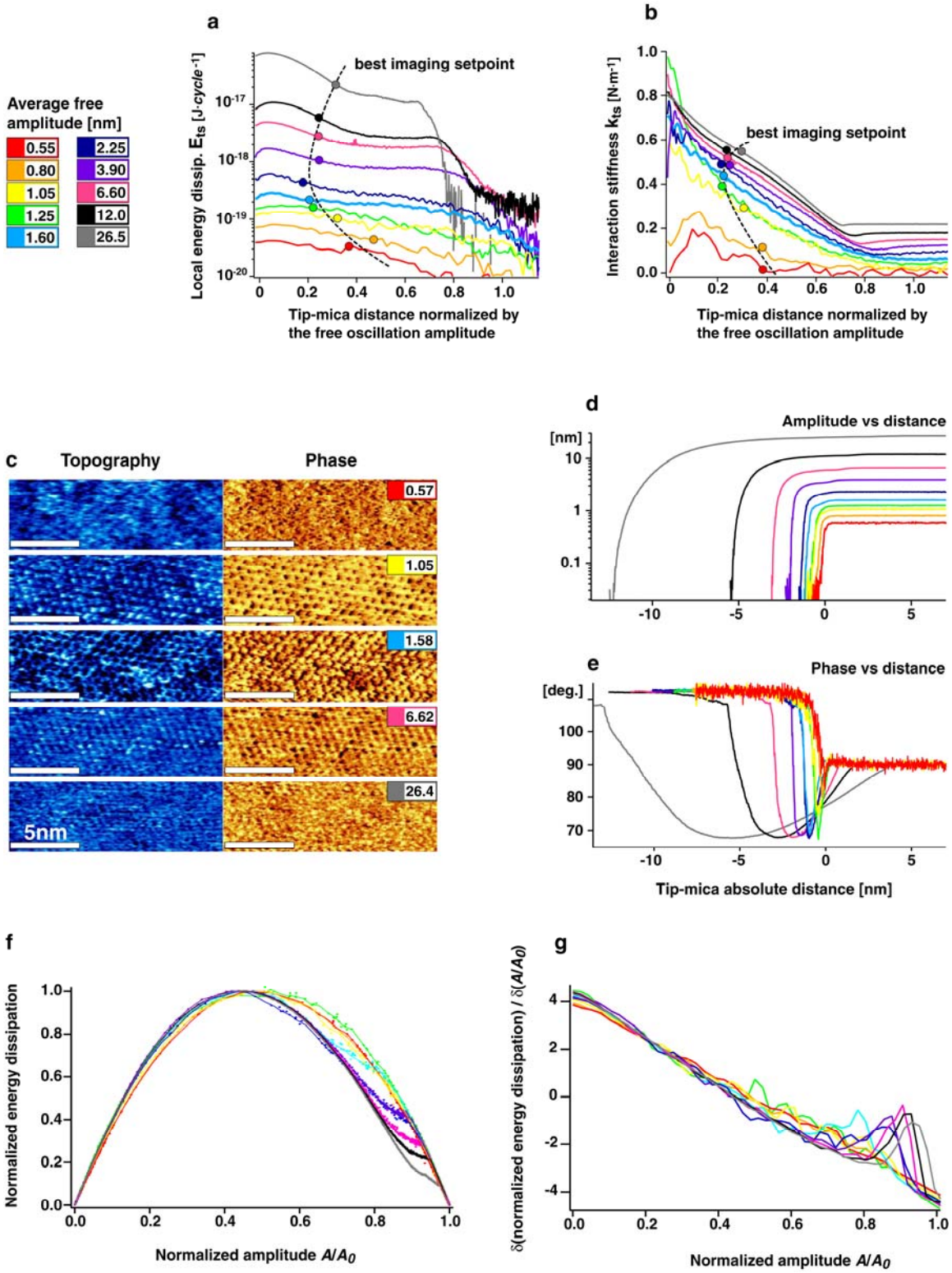

Figure S1: supplementary information to Fig. 1 and identification of the main energy dissipation mechanism (see text for details)

No bistability or branching in the curves (from distinct attractive or repulsive modes commonly observed in non-liquid environment[5]) was observed in these amplitude curves. In order to confirm the nature of the main energy dissipation mechanism (damping into the interfacial liquid) we analyzed our results in the framework developed by Garcia et al. which distinguishes between three main dissipation processes: surface energy hysteresis, viscoelasticity, and long-range dissipative interfacial interactions[11]. Although this theory was verified in air[11], it can provide valuable insight into the energy dissipation mechanism likely to dominate in the present case since the interfacial liquid can be seen as a viscoelastic layer at the surface of the solid substrate.

The appropriate plots are presented in Fig. S1 (f) and (g) showing the normalized energy dissipation (f) and its first derivative (g) plotted against the corresponding normalized amplitude as the tip approaches the sample. In (f) the experimental data is represented by dots and the curves were obtained by linear interpolation. In (g), the curves were obtained by differentiating the interpolated curves (in (f)) with respect to the corresponding normalized amplitude. For free oscillation amplitudes $A_0 < A_{0,\ optimum}$, the energy dissipation mechanism appears best described by viscoelstacity. This is particularly clear when considering the near-linear derivative of the normalized E_{TS} (g). However, the lack of inflexion points in the normalized E_{TS} *vs* A/A_0 curves (f) suggests that of long-range dissipative interfacial interactions could also play a role in the energy dissipation. For free oscillation amplitudes $A_0 \geq A_{0,\ optimum}$, the normalized E_{TS} curves appear less symmetric with a progressively marked shoulder as A_0 increases. This shoulder leads to a transition in the E_{TS} curves' derivative (g) suggesting the emergence of surface energy hysteresis. This effect, more marked for larger amplitudes, can be explained by the tip

directly interacting with the mica substrate (nanoindentation). However, under optimal imaging conditions, the energy dissipation mechanism appears dominated by the viscoelasticity of the interfacial liquid.

3. Modification of the mica-water interface by adjunction of ions in solution

When the tip approaches the solid, its vibration is damped according to two distinct regimes (Fig. 1c and S1 and SI section 1).

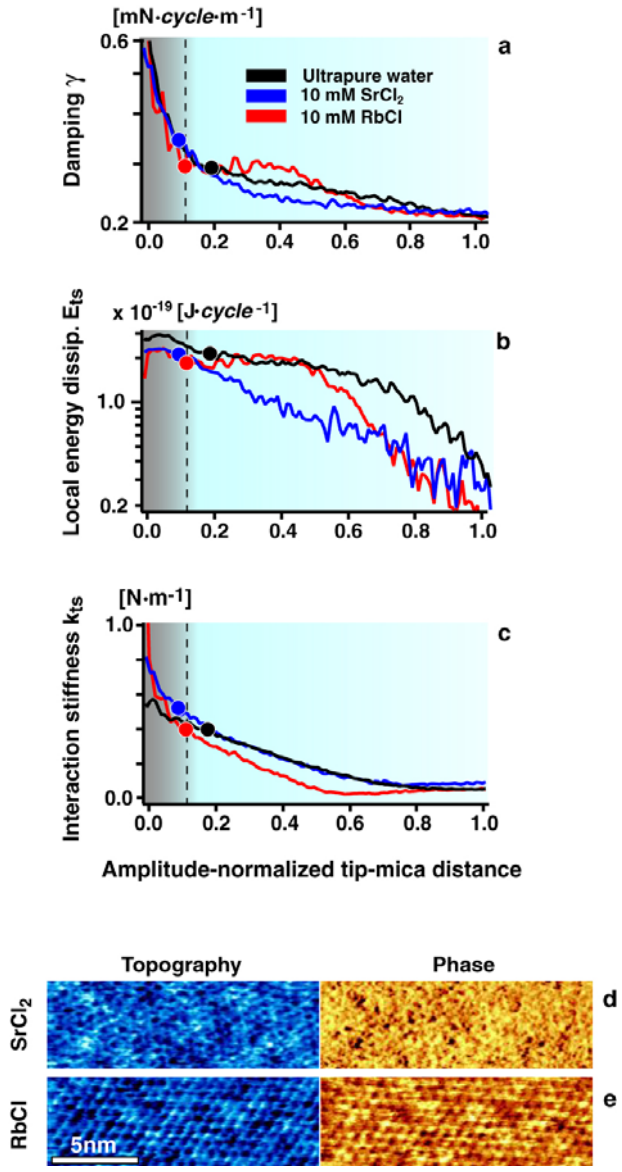

Figure S2: Mica-water interface in the presence of different salts (see text for details). The dotted vertical line suggests the transition between interfacial liquid (blue background) and the mica (darker background)

We interpreted these two regimes as dominated by the interfacial liquid and the substrate respectively. In the damping vs. distance curves (Fig. 1c) the transition between the two regimes is identified by a change in slope as the tip moves closer to the substrate.

In order to confirm this interpretation, we modified the properties of the interfacial liquid through the adsorption or coordination of different ions known to adsorb at various distances from the mica itself[18], therefore strongly affecting the interfacial liquid in comparison with pure water on mica. The free amplitudes allowing the best resolution during imaging in these solutions were similar to that for mica in ultrapure water (1.44 nm for RbCl, 1.46 nm for $SrCl_2$, peak-to-peak free amplitude Fig. S2c) thus allowing meaningful comparison of the imaging parameters. The damping curves (Fig. S2a) show substantial differences for the different samples in the regime interpreted as due to the interfacial liquid whereas the mica-dominated regime is nearly identical in all cases. A full study of ion-related solvation effects is beyond the scope of this paper, but these results nevertheless confirm our initial interpretation of the damping curves in Fig. 1c.

4. Supplementary high-resolution images and controls

Figure S3 presents supplementary high-resolution data and controls carried out to ensure reliability of the images presented in Fig. 2.

In each case, the topographic image appears in blue scale and the phase image in red-yellow scale as in the manuscript's figures. The upper part of Fig. S3 shows high-resolution images of 1,2-dihexadecanoyl-sn-glycero-3-phosphate (sodium salt) (DPPA) and 1,2-dihexadecanoyl-sn-glycero-3-phospho-L-serine (sodium salt) (DPPS) lipid bilayers. The existence of a true bilayer was always verified by nanodissection, as exemplified for DPPC. The bilayer could be mechanically removed by scanning the surface under harsh conditions (low setpoint, low feedback gains, high-speed). The DPPA and DPPS images were acquired in 20mM NaCl solution as for the DPPC bilayer presented in Fig. 2. High resolution imaging on DPPC could also be achieved in PBS buffer (images of DPPC presented in Fig. S3). The molecular structure of the different lipid head-groups is also given.

The lower part of Fig. S3 presents lower magnification images of the crystals shown in Fig. 2. The images given in Fig. 2 have also been added for comparison. It can clearly be seen that the features visible in the high-resolution images appear smaller in the lower magnification frames and are consequently real. All the images presented in the lower part of Fig. 3 were acquired in dimethylsulfoxide (DMSO)

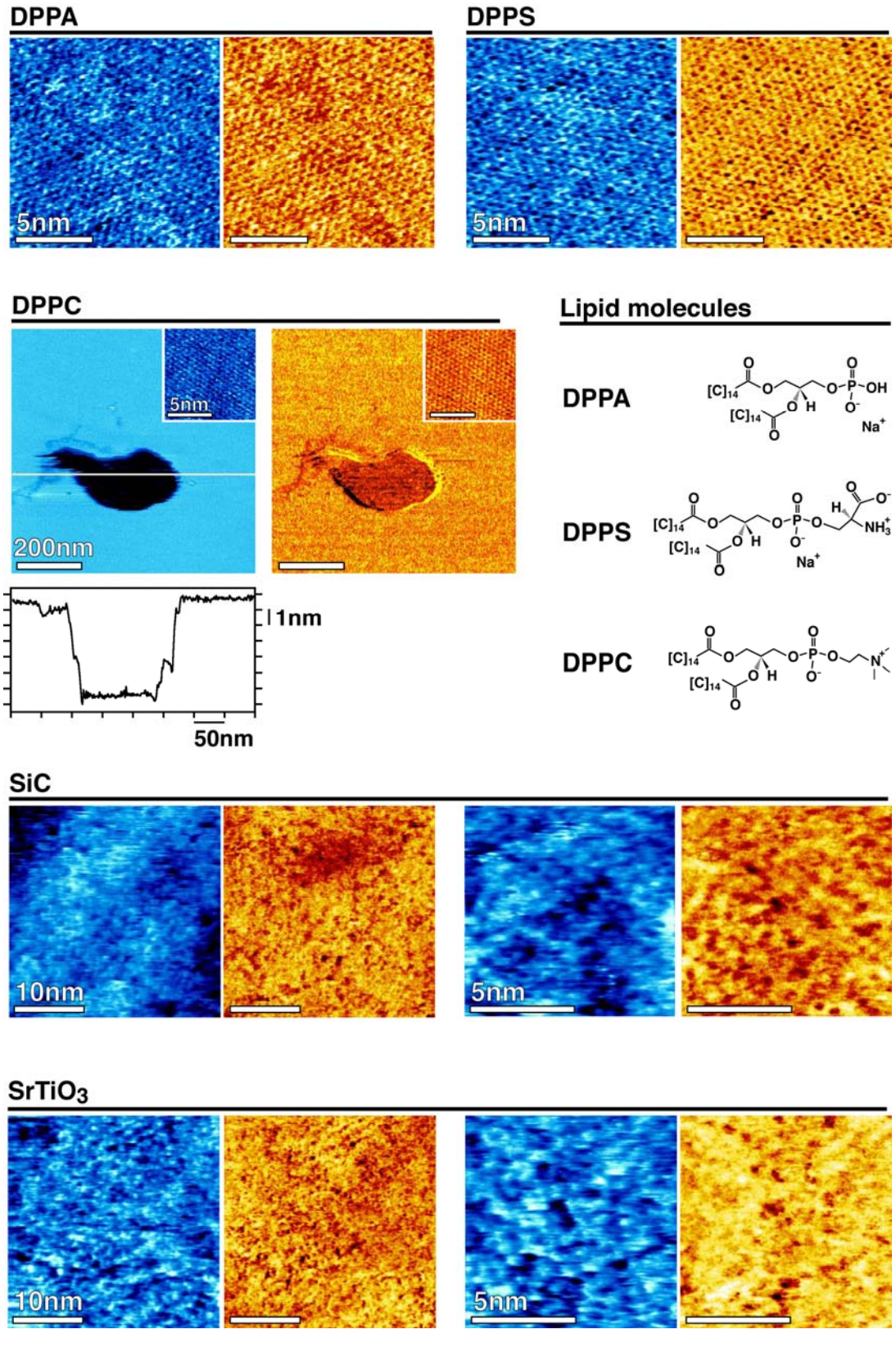

Figure S3: Control experiments and supplementary data to Fig. 2 (see text)

6. Derivation of the model for calculating the substrate-liquid work of adhesion and supplementary discussion

Definition of the work of adhesion and general considerations

The physical meaning of the particular conditions allowing high-resolution imply the possibility to derive further information from the imaging parameters, in particular the sample-liquid local work of adhesion (or adhesion energy) W_{SL}. W_{SL} is defined as the free energy cost per unit surface area to separate the solid from the liquid. Experimentally, W_{SL} is a meaningful value to quantify the interface at any scale as it only depends on the solid and the liquid molecular properties[19]. It is related to the interfacial energy γ_{SL} (S=solid, L=liquid, V=vapour) and both medias' surface energies (γ_S and γ_L respectively) by the *Dupré* equation[20]:

$$\gamma_{SL} = \gamma_S + \gamma_L - W_{SL} \qquad \textbf{(s1)}$$

Given that the surface energies are constant for each medium, the work of adhesion W_{SL} and γ_{SL} describe a same concept. Experimentally, W_{SL} is usually measured with the contact angle θ_{CA} formed by static, macroscopic liquid droplets at the surface of a flat solid in an inert atmosphere using the so-called *Young-Dupré* equation $W_{SL} = \gamma_{LV}(1 + \cos\theta_{CA}) \approx \gamma_L(1 + \cos\theta_{CA})$[21]. However, it is effectively averaged over the triple line bordering the solid, liquid and vapour regions[22,23]. At a microscopic scale, several AFM studies have indirectly deduced W_{SL} either from the static adhesion force between an AFM tip and a solid surface in a liquid or vapor[24-27] or through microscopic contact angle measurements obtained from AFM scans of nanoscale droplets[28,29], but to the best of our knowledge never with sub-nanoscale lateral resolution. Here we directly relate the tip

local energy dissipation during the capture of high-resolution images with both the tip and the sample's work of adhesion with the liquid (W_{TL} and W_{SL} respectively).

Implications for the model

Before presenting the model in detail, it is useful to realize that work of adhesion represents, by definition, the global interaction energy between the different media; if both media are identical, then the interfacial energy is simply two times the surface energy of the medium and the work of adhesion is zero. The work of adhesion therefore represents the energy responsible for interfacial restructuring. In the case of a solid-liquid interface, the restructuring will occur almost only in the liquid due to the mobility of the liquid molecules (i.e. $\gamma_S >> \gamma_L$). This restructuring will however occur over a finite distance (typically a few molecular diameters[30-32]) and the liquid density excess (compared to bulk) will tend to vanish away rapidly from the interface. The exact shape of this decay can be complex with sudden transition between hydration layers[33] and generally depends on both the solid and the liquid. Several experimental studies (mostly AFM and surface force apparatus) confining liquid between two solids have found a decay satisfactorily modelled with an modulated exponential function[31,32,34-37]. A direct interpretation of these results in terms of interfacial liquid density variation should however be done with care since confinement effects could also influence the observed trends[32,33]. Nevertheless, we modelled the gradient of W_{SL} when moving away from the surface ($\partial W_{SL}/\partial z$) as decaying exponentially and approaching its asymptotic value of zero over a few molecular diameters (see Fig. 1d and S5). The effective repulsive force felt by the tip as it approaches the surface is consequently a composition of both exponentially

decaying interfaces interpenetrating. The measured energy dissipation spent during the first part of the oscillation (approach) is assumed to be the energy necessary to partially destroy both the tip and the sample interface by forming a common interface. Taking into account the geometry of the system (assumed to be plane-parabola) and integrating the work accomplished by the tip over the approach it is possible to relate the corresponding energy dissipated by the tip with W_{SL} and W_{TL}. However, since the work of adhesion is by definition reversible, if the process is adiabatic no energy should be effectively dissipated during a full oscillation cycle (approach+retraction, see Fig. S4a below). Experimentally, we measure an energy dissipation that scales with W_{SL} as the tip oscillates in the interfacial liquid. We explain this dissipation by a deviation from the adiabatic case (area E_3 in Fig. S4b) induced by the viscoelasticity of the interfacial liquid. In other words, the timescale of the measurement does not allow for the interfacial liquid to fully relax, leading to a hysteresis loop which surface which is (i) the measured energy dissipation and (ii) proportional to an average of the tip and sample works of adhesion with the liquid (see development below). The exact shape of the tip oscillation trajectory (schematized in Fig. S4b) is experimentally very challenging to determine. Consequently, a fully accurate and theoretically sound model that relates the measured experimental parameters with the interface thermodynamic quantities remains to be developed.

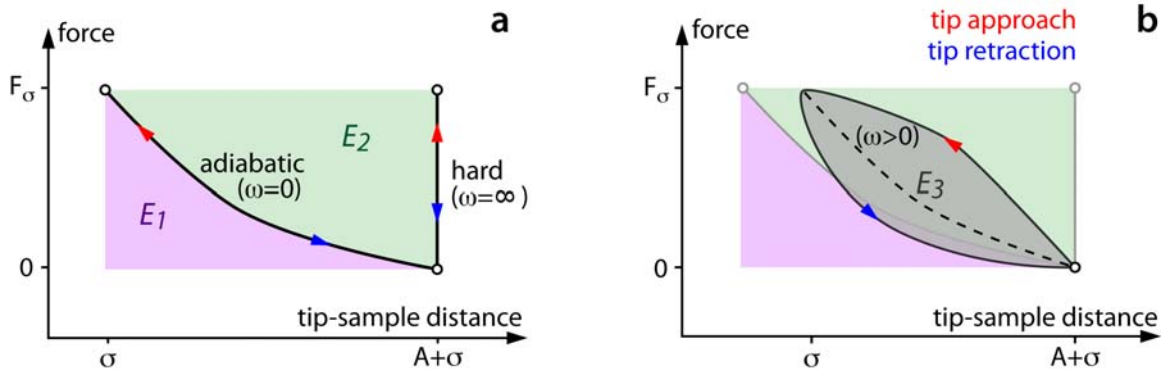

Figure S4: (a) Scheme of two limit cases of tip oscillation trajectories. The "hard" trajectory corresponds to the case where the tip meets an infinitely hard interface. This is the case for an infinitely fast oscillation where the interfacial liquid can be seen as a glass (ω=∞). The "adiabatic" trajectory represents a quasi-static trajectory of the tip with the process slow enough to be reversible (no viscous loss, ω=0). In each case no energy is dissipated. E_1 is the area below the adiabatic trajectory and E_2 the area between the two trajectories. A is the tip oscillation amplitude and σ the smallest tip-sample distance. A more realistic tip oscillation trajectory is presented in (b). The centre of the tip trajectory (dotted line) appears steeper than for the adiabatic case ($\omega=\omega_{experiment}>0$). Due to the liquid viscoelasticity the approach and retraction trajectory deviate in opposing directions from the dotted trajectory, thus forming a hysteresis loop (grey area labelled E_3) corresponding to the energy dissipated by the tip during an oscillation cycle.

In the absence of a full theoretical description of the system, we developed a model reflecting an ideal case: if the adiabatic trajectory (Fig. S4a) is considered in first approximation linear, then the area $E_1 \sim E_2$ (Fig. S4a) and the measured energy dissipation E_{TS} admits $E_1+E_2 \sim 2E_1$ as an upper limit. In the model presented bellow, we

assume that E_1 is proportional to E_{TS} ($E_1 = \lambda E_{TS}$). We then calculate E_1 as a function of the tip-liquid and substrate-liquid works of adhesion.

The model (adiabatic tip-substrate approach with soft retraction)

For the sake of clarity, the basic assumptions of the model are summarized below:

1. The re-structuring of the liquid at the solid-liquid interface fully accounts for the interfacial energy. A direct consequence of this assumption is that probing the liquid down to its first hydration layer is sufficient to quantitatively measure the work of adhesion (as in CA measurements).
2. The effective interface (as opposed to bulk) is fully located in the liquid. The so-defined "interface" can be modelled as decaying exponentially into the bulk liquid[30,31]. The exponential factor α would then typically be a few molecular diameters.
3. The solid surface is locally flat compared to the AFM tip which is assumed to be parabolic. This is on the scale of the tip size R (parabola of equation $z=(x+y)^2/2R$ with x,y parallel to the interface and z perpendicular)[35]
4. At each tap, the tip motion is assumed to be purely in the z direction (lateral scan speed $v_{x,y}$ neglected since $v_{x,y} << v_z$).
5. The AFM amplitude is relatively small, i.e. comparable to the width of the total surface-liquid-tip interface and the whole system has circular symmetry (around the z axis). Moreover, the tip never touches the actual surface, but there is always at least one molecular diameter of liquid between tip and surface. (This last affirmation is experimentally suggested in typical amplitude curves, but only if the liquid adheres

The situation is illustrated in Fig. 1d and in Fig. S5 below.

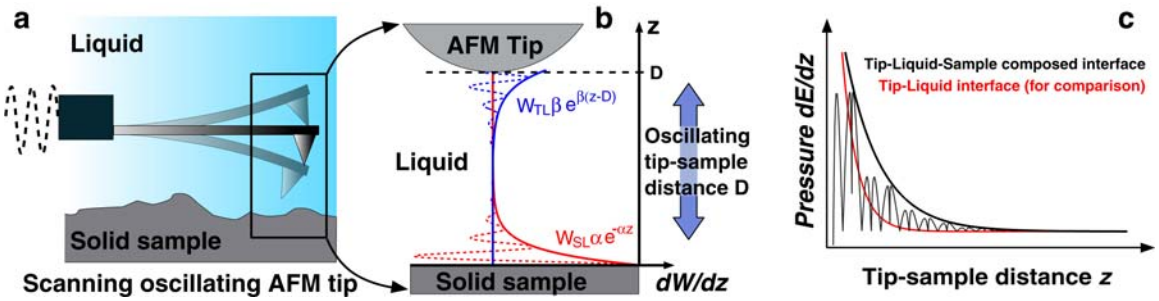

Figure S5: Scheme of the tip-liquid-sample system in the model for calculating W_{SL}.

Fig. S5b shows schematically the density of interfacial energy at both the tip and the sample interface with the liquid. At both interfaces the density of the work of adhesion (which takes the unit of pressure) can be modelled by:

$$P_{SL}(z) = W_{SL}\alpha e^{-\alpha z}$$
$$P_{TL}(z, D) = W_{TL}\beta e^{\beta(z-D)} \qquad \textbf{(s2)}$$

with the index S and T for the solid sample and the tip respectively, and α and β the exponential decay length at the sample and the tip respectively. D is the tip-sample

distance along the z axis. P_{SL} and P_{TL} are such that if integrated along z from z=0 (solid surface) to infinity, the result is exactly the work of adhesion between the liquid and the surface considered. P_{SL} and P_{TL} are the exponential curves appearing in red and blue respectively in Fig S5b. The pressure P_{TLS} met by the tip when approaching the sample is then obtained considering the maximum value of pressure among the crossing points between P_{SL} and P_{TL} for a given distance D between the tip and the sample:

$$P_{TLS}(D) \equiv P_{SL}(z_D) \text{ with } z_D \;\middle|\; P_{SL}(z_D) = \max\left\{ P_{SL}(z) \;\middle|\; P_{SL}(z) = P_{TL}(z), z \in [0, D] \right\} \quad \textbf{(s3)}$$

When considering only the exponential envelope of P_{SL} and P_{TL} (as in eq. (s2)), this yields to

$$P_{TLS}(D) = [W_{SL}\alpha]^{\frac{\beta}{\alpha+\beta}} [W_{TL}\beta]^{\frac{\alpha}{\alpha+\beta}} e^{\frac{-\alpha\beta}{\alpha+\beta}D} \quad \textbf{(s4)}$$

The thick black curve in Fig. S5c was plotted from eq. (s4) while the oscillatory-like thinner dark curve is derived numerically from definition (s3) using the assumed P_{TL} and P_{SL} pair curves for the tip and the sample interfaces with the liquid in Fig. S5b. P_{SL} (in red) is also plotted for comparison in Fig. S5c. The advantage of this approach is that it allows a simple description of the work of adhesion while remaining compatible, at least qualitatively with the AFM and surface force apparatus (SFA) experiments at solid-liquid interface which reported oscillatory behaviour for P_{TLS}[31,32,35-37]. Here, we assume the exponentially decaying behaviour is solely dependent of the solvent, hence α=β. This assumption, also compatible with published literature[31,32,35-37] is a simplification of reality[33].

Using the assumption 1-5, the energy dissipation per cycle can be obtained by summing $P_{TLS}(D)$ over the surface elements of the tip. For a parabolic shaped tip over a flat surface ($z = D + y^2/2R$ with y along the surface plane) the summation can be obtained by adapting the Derjaguin approximation[31] to the plane-parabola case[35]. The energy dissipation per cycle is then given by integrating P_{TLS} over the surface elements of the tip and over a tip sample approach:

$$E_{cycl,ext} = \int_0^{\infty} \int_{\sigma}^{A+\sigma} 2\pi y P_{TLS}(z) dD dy = \frac{8\pi R}{\alpha} \sqrt{W_{SL} W_{TL}} e^{\frac{-\alpha}{2}\sigma} \left(1 - e^{\frac{-\alpha}{2}A}\right) \qquad \textbf{(s5)}$$

with σ a molecular diameter of the liquid, A the tip amplitude and R the local tip radius.

No additional dissipation term is assumed for the retracting phase of the tip (soft trajectory). Equation (s5) can then be combined with the energy dissipation E_{TS} calculated from scanning parameters[5,6,10-12] ($E_{cycl,ext} = E_1 = \lambda E_{TS}$) to effectively relate the W_{SL} with the experimental parameters (W_{TL} is measured independently):

$$W_{SL} = \frac{\lambda^2}{W_{TL}} \left(\frac{k_L \alpha A_0^2}{8RQ} \frac{\left[\frac{A}{A_0} \sin\varphi - \left(\frac{A}{A_0} \right)^2 \right]}{\left[e^{-\frac{\alpha}{2}\sigma} - e^{-\frac{\alpha(A+\sigma)}{2}} \right]} \right)^2 \qquad \textbf{(s6)}$$

This formula was employed to calculate the work of adhesion of the different samples studied throughout this paper. We took σ = 2Å for water and σ = 3Å for DMSO. We arbitrarily chose 1/α=3/2σ as it appears a good compromise with the available literature values[30,31,35] and A is the AFM scanning amplitude. The local tip radius R was assumed to be 2nm. This radius value was obtained by considering the effective tip radius able to

provide the lateral resolution demonstrated here, given a force field decaying exponentially with $\alpha/2$ (eq. s4). Practically, asperities and surface defects at the apex of the tip are probably responsible for the high-resolution achieved. Finally, we found values for the proportionality coefficient λ ranging between 0.74 to 1.16 depending on the solvent (from the slope of the curves in Fig. 3).

This model is however simplistic and cannot fully capture the true complexity of the tip motion in liquid[14,38,39]. Furthermore, several underlying assumptions employed in the model may not be always valid. First the system's geometry (tip and sample shape) and the use of the Derjaguin approximation can over-simplify the reality[40]. Second, liquids can present significant changes in their apparent viscosity when confined[41,42] and further improvements of the model may require precisely quantifying the liquid's viscoelastic relaxation under the scanning conditions. Third, the reciprocal influence of the tip and the sample on the sample-liquid and tip-liquid interfaces, respectively, are not taken into account and both interfaces are assumed to remain structurally constant while interpenetrating each other. This assumption becomes particularly problematic if there is a large difference in the liquid's affinity for the tip and for the substrate. Modelling the interfacial energy losses utilizing the probability of the oscillating tip to create nanoscale cavities near the interface[43] may ultimately provide better results. Finally, the model does not take into account lateral friction forces responsible for the image formation in contact mode. The vibration velocity of the tip in the *z*-direction is however always 1-2 orders of magnitude higher than the scanning velocity and high-resolution imaging was possible over a wide range of speed (~40nm/s to ~500nm/s), although higher scan speeds were preferred to minimize drift.

Despite its simplicity, the model presented here was able to provide correct estimates for W_{SL} for most samples studied after calibration with contact angle values (see Fig. 3), suggesting that it can capture the fundamental tip dissipation mechanism at the solid-liquid interface.

8. Supplementary references

1. Liang, Y., Lea, A. S., Baer, D. R. et al., Structure of the cleaved CaCO3(1014) surface in an aqueous environment. *Surf. Sci.* **351** (1-3), 172 (1996).
2. Rinia, H. A., Kik, R. A., Demel, R. A. et al., Visualization of Highly Ordered Striated Domains Induced by Transmembrane Peptides in Supported Phosphatidylcholine Bilayers. *Biochemistry* **39** (19), 5852 (2000).
3. Kuna, J. J., Voitchovsky, K., Singh, C. et al., The effect of nanometre-scale structure on interfacial energy. *Nat. Mater.* **8** (10), 837 (2009).
4. Pethica, J. B. and Oliver, W. C., Tip Surface Interactions in STM and AFM. *Physica Scripta* **T19A**, 61 (1987).
5. García, R. and Pérez, R., Dynamic atomic force microscopy methods. *Surf. Sci. Rep.* **47** (6-8), 197 (2002).
6. Cleveland, J. P., Anczykowski, B., Schmid, A. E. et al., Energy dissipation in tapping-mode atomic force microscopy. *Appl. Phys. Lett.* **72** (20), 2613 (1998).
7. Patil, S. V. and Hoffmann, P. M., Small-Amplitude Atomic Force Microscopy. *Adv. Eng. Mater.* **7** (8), 707 (2005).
8. Hoffmann, P. M., (CRC Press, 2004).
9. Hoffmann, P. M., Jeffery, S., Pethica, J. B. et al., Energy dissipation in atomic force microscopy and atomic loss processes. *Phys. Rev. Lett.* **87** (26) (2001).
10. Anczykowski, B., Gotsmann, B., Fuchs, H. et al., How to measure energy dissipation in dynamic mode atomic force microscopy. *Appl. Surf. Sci.* **140** (3-4), 376 (1999).
11. Garcia, R., Gomez, C. J., Martinez, N. F. et al., Identification of Nanoscale Dissipation Processes by Dynamic Atomic Force Microscopy. *Phys. Rev. Lett.* **97** (1), 016103 (2006).
12. Garcia, R., Magerle, R., and Perez, R., Nanoscale compositional mapping with gentle forces. *Nat. Mater.* **6** (6), 405 (2007).
13. Melcher, J., Carrasco, C., Xu, X. et al., Origins of phase contrast in the atomic force microscope in liquids. *Proc. Natl. Acad. Sci. U. S. A.* **106** (33), 13655 (2009).
14. Melcher, J., Hu, S., and Raman, A., Invited Article: VEDA: A web-based virtual environment for dynamic atomic force microscopy. *Rev. Sci. Inst.* **79** (6), 061301 (2008).
15. Xu, X., Melcher, J., Basak, S. et al., Compositional Contrast of Biological Materials in Liquids Using the Momentary Excitation of Higher Eigenmodes in Dynamic Atomic Force Microscopy. *Phys. Rev. Lett.* **102** (6), 060801 (2009).
16. Kuwahara, Y., Muscovite surface structure imaged by fluid contact mode AFM. *Phys. Chem. Minerals* **26** (3), 198 (1999).
17. Fukuma, T., Kilpatrick, J. I., and Jarvis, S. P., Phase modulation atomic force microscope with true atomic resolution. *Rev. Sci. Inst.* **77** (12), 123703 (2006).
18. Fenter, P., Park, C., Nagy, K. L. et al., Resonant anomalous X-ray reflectivity as a probe of ion adsorption at solid-liquid interfaces. *Thin Sol. Films* **515** (14), 5654 (2007).

19. Zhang, J. and Kwok, D. Y., Combining Rule for Molecular Interactions Derived from Macroscopic Contact Angles and Solid-Liquid Adhesion Patterns. *Langmuir* **19** (11), 4666 (2003).
20. Dupré, A., *Théorie mécanique de la chaleur*. (Gauthier-Villars, Paris, 1869).
21. Young, T., An Essay on the Cohesion of Fluids. *Philosophical Transactions of the Royal Society of London* (1804).
22. Tadmor, R., Line Energy and the Relation between Advancing, Receding, and Young Contact Angles. *Langmuir* **20** (18), 7659 (2004).
23. Amirfazli, A. and Neumann, A. W., Status of the three-phase line tension: a review. *Adv. Coll. Interf. Sci.* **110** (3), 121 (2004).
24. Vezenov, D. V., Zhuk, A. V., Whitesides, G. M. et al., Chemical Force Spectroscopy in Heterogeneous Systems:Intermolecular Interactions Involving Epoxy Polymer, Mixed Monolayers, and Polar Solvents. *J. Am. Chem. Soc.* **124** (35), 10578 (2002).
25. Drelich, J., Tormoen, G. W., and Beach, E. R., Determination of solid surface tension from particle-substrate pull-off forces measured with the atomic force microscope. *J. Coll. Interf. Sci.* **280** (2), 484 (2004).
26. Beach, E. R., Tormoen, G. W., and Drelich, J., Pull-off forces measured between hexadecanethiol self-assembled monolayers in air using an atomic force microscope: analysis of surface free energy. *J. Adh. Sci. Tech.* **16**, 845 (2002).
27. Butt, H.-J., Cappella, B., and Kappl, M., Force measurements with the atomic force microscope: Technique, interpretation and applications. *Surf. Sci. Rep.* **59** (1-6), 1 (2005).
28. Checco, A., Schollmeyer, H., Daillant, J. et al., Nanoscale Wettability of Self-Assembled Monolayers Investigated by Noncontact Atomic Force Microscopy. *Langmuir* **22** (1), 116 (2006).
29. Checco, A., Cai, Y., Gang, O. et al., High resolution non-contact AFM imaging of liquids condensed onto chemically nanopatterned surfaces. *Ultramicro.* **106** (8-9), 703 (2006).
30. Widom, B., Intermolecular Forces and the Nature of the Liquid State: Liquids reflect in their bulk properties the attractions and repulsions of their constituent molecules. *Science* **157**, 375 (1967).
31. Israelachvili, J. N., *Intermolecular and Surface Forces, Second Edition: With Applications to Colloidal and Biological Systems*, 2nd ed. (Academic Press, 1992).
32. Israelachvili, J. and Wennerstrom, H., Role of hydration and water structure in biological and colloidal interactions. *Nature* **379** (6562), 219 (1996).
33. Fenter, P. and Sturchio, N. C., Mineral-water interfacial structures revealed by synchrotron X-ray scattering. *Prog. Surf. Sci.* **77** (5-8), 171 (2004).
34. Lantz, M., Liu, Y. Z., Cui, X. D. et al., Dynamic force microscopy in fluid. *Surf. Interf. Anal.* **27** (5-6), 354 (1999).
35. O'shea, S. J., Welland, M. E., and Pethica, J. B., Atomic-Force Microscopy of Local Compliance at Solid-Liquid Interfaces. *Chem. Phys. Lett.* **223** (4), 336 (1994).
36. O'Shea, S. J. and Welland, M. E., Atomic force microscopy at solid-liquid interfaces. *Langmuir* **14** (15), 4186 (1998).

37. O'Shea, S. J., Lantz, M. A., and Tokumoto, H., Damping near Solid-Liquid Interfaces Measured with Atomic Force Microscopy. *Langmuir* **15** (4), 922 (1999).
38. Couturier, G., Aimé, J. P., Salardenne, J. et al., A virtual non contact-atomic force microscope (NC-AFM): Simulation and comparison with analytical models. *Eur. Phys. J. Appl. Phys.* **15** (2), 141 (2001).
39. Martin, M. J., Fathy, H. K., and Houston, B. H., Dynamic simulation of atomic force microscope cantilevers oscillating in liquid. *J. Appl. Phys.* **104** (4), 044316 (2008).
40. Lim, L. T. W., Wee, A. T. S., and O'Shea, S. J., Effect of Tip Size on Force Measurement in Atomic Force Microscopy. *Langmuir* **24** (6), 2271 (2008).
41. Zhu, Y. and Granick, S., Viscosity of Interfacial Water. *Phys. Rev. Lett.* **87** (9), 096104 (2001).
42. Li, T.-D. and Riedo, E., Nonlinear Viscoelastic Dynamics of Nanoconfined Wetting Liquids. *Phys. Rev. Lett.* **100** (10), 106102 (2008).
43. Godawat, R., Jamadagni, S. N., and Garde, S., Characterizing hydrophobicity of interfaces by using cavity formation, solute binding, and water correlations. *Proc. Natl. Acad. Sci. U. S. A.* **106** (36), 15119 (2009).